Bioactive Materials 13 (2022) 82–95

Contents lists available at ScienceDirect

Bioactive Materials

journal homepage: www.keaipublishing.com/en/journals/bioactive-materials

# A regeneration process-matching scaffold with appropriate dynamic mechanical properties and spatial adaptability for ligament reconstruction

Xiaojing Xie [a,1], Junjie Xu [b,1], Jing Lin [a], Jia Jiang [b], Yunfan Huang [a], Jun Lu [a], Yuhao Kang [b], Yage Hu [a], Jiangyu Cai [b], Fujun Wang [a], Tonghe Zhu [b,**], Jinzhong Zhao [b,***], Lu Wang [a,*]

[a] Key Laboratory of Textile Science & Technology of Ministry of Education, College of Textiles, Donghua University, Shanghai, 201620, China
[b] Department of Sports Medicine, Department of Orthopedics, Shanghai Jiao Tong University Affiliated Sixth People's Hospital, Shanghai, 200233, China

ARTICLE INFO

*Keywords:*
Ligament
Regeneration process
Fiber
Dynamic mechanical property
Allowable space

ABSTRACT

Ligament regeneration is a complicated process that requires dynamic mechanical properties and allowable space to regulate collagen remodeling. Poor strength and limited space of currently available grafts hinder tissue regeneration, yielding a disappointing success rate in ligament reconstruction. Matching the scaffold retreat rate with the mechanical and spatial properties of the regeneration process remains challenging. Herein, a scaffold matching the regeneration process was designed via regulating the trajectories of fibers with different degradation rates to provide dynamic mechanical properties and spatial adaptability for collagen infiltration. This core-shell structured scaffold exhibited biomimetic fiber orientation, having tri-phasic mechanical behavior and excellent strength. Besides, by the sequential material degradation, the available space of the scaffold increased from day 6 and remained stable on day 24, consistent with the proliferation and deposition phase of the native ligament regeneration process. Furthermore, mature collagen infiltration and increased bone integration *in vivo* confirmed the promotion of tissue regeneration by the adaptive space, maintaining an excellent failure load of 67.65% of the native ligament at 16 weeks. This study proved the synergistic effects of dynamic strength and adaptive space. The scaffold matching the regeneration process is expected to open new approaches in ligament reconstruction.

## 1. Introduction

Ligaments are responsible for the mechanical transmission of forces from bones to bones. Ligament tissues are composed of highly oriented crimped collagen fiber bundles wrapped by synovium, exhibiting considerable tri-phasic mechanical properties and excellent axial tensile strength and stiffness [1–3]. Ligament rupture occurs when the applied load exceeds its strength. It is reported that the annual cost of ligament rupture repairs accounts for tens of billions of dollars in Western countries [3,4]. Ligament regeneration is a sophisticated process, and it can be primarily divided into three overlapping phases. The duration of these phases depends on the location and severity of the disease. The initial phase is an inflammatory reaction, which begins with the formation of a temporary hematoma shortly after rupture and usually disappears within 1 week [5–7]. The proliferation phase occurs from 5 to 7 days after injury, accompanied by the synthesis and deposition of ECM components at the wound site [8–10]. According to the patient's conditions, the remodeling phase begins 6–8 weeks after injury and lasts for months or even years [11,12]. Therefore, an ideal engineered scaffold for ligament reconstruction should provide dynamic mechanical support and allowable space to accommodate these three physiological phases.

Currently, the selection of grafting materials is very challenging. Grafting materials should endow alternatives with matching mechanical

Peer review under responsibility of KeAi Communications Co., Ltd.
* Corresponding author.
** Corresponding author. Department of Sports Medicine, Department of Orthopedics, Shanghai Jiao Tong University Affiliated Sixth People's Hospital, No. 600 Yishan Road, Shanghai, 200233, China.
*** Corresponding author. Department of Sports Medicine, Department of Orthopedics, Shanghai Jiao Tong University Affiliated Sixth People's Hospital, No. 600 Yishan Road, Shanghai, 200233, China.
*E-mail addresses:* zhutonghe@sjtu.edu.cn (T. Zhu), jzzhao@sjtu.edu.cn (J. Zhao), wanglu@dhu.edu.cn (L. Wang).
[1] These authors contributed equally to this work.

https://doi.org/10.1016/j.bioactmat.2021.11.001
Received 11 August 2021; Received in revised form 2 November 2021; Accepted 2 November 2021
Available online 12 November 2021

properties and adaptive space. Carbon-based Intergraft, polytetrafluoroethylene (PTFE)-based Gore-Tex, and polyethylene terephthalate (PET)-based Leeds-Keio were reported as synthetic fiber scaffolds with excellent mechanical strength, which even exceeds that of ligaments in humans, exhibiting favorable short-term clinical results. Disappointingly, various complications with these artificial implantations were reported, such as synovitis and long-term graft rupture, which was a combined effect of various factors including failure to provide suitable biological tissue ingrowth into the scaffold structure resulting from their poor biocompatibility and compact structure, then chronic inflammatory response caused by non-degradable wear particles generated by friction, and poor long-term mechanical performance originating from the unsuccessful remodeling of collagen fibers caused by stress shielding effect [4,13–15]. A PET-based ligament advanced reinforcement system (LARS) is a synthetic device currently used in the clinic. However, recent studies have shown a 33.3% failure rate of anterior cruciate ligament (ACL) reconstruction with LARS after 3.9 years of follow-up [16–18]. The proliferative fibrous tissue caused by the chronic inflammatory wrapped the scaffold and prevented the infiltration of new tissue, yielding the reconstruction failure [8,16,18–20]. Apparently, a group of strong and straight fibers is not sufficient for a successful and effective ligament substitute.

Biodegradable materials are considered promising ligament device materials since non-biodegradable devices showed unsatisfactory results. Their biodegradation enables the removal of the scaffold material and its gradual replacement by new tissue, which is vital for tissue regeneration. Different degradable materials possess distinct mechanical properties, degradation rates, and cellular responses of customized scaffolds. Natural cell-friendly biodegradable materials, such as collagen [21,22], hyaluronic acid [23], and alginate [24,25], have been used for ligament regeneration, but their poor mechanical properties and fast degradation rate led to premature failure of scaffolds. In recent years, synthetic biodegradable polymers with good mechanical properties, such as polyurethane (PU), polylactic acid (PLA), polycaprolactone (PCL), poly(*p*-dioxanone) (PPDO), polyglycolic acid (PGA), and their copolymers, have shown great promise [8]. Fiber-based scaffolds have become a research hotspot in recent years based on the in-depth understanding of the ligaments' fiber structure. The developed technologies for producing fiber-based scaffolds include wire-rope, braiding, knitting, weaving, and electrospinning [26]. Braiding, which provides porous structures with high uniaxial tensile strength and tri-phasic mechanical behavior, and electrospinning, which can yield micrometer fibers, were combined to closely replicate anatomical and mechanical characteristics of ligaments [27–29]. Despite the promising idea, tissue ingrowth in the synthesized scaffolds was limited due to the lack of allowable space resulting from slow scaffold retreat. Bone dissolution and graft fracture phenomena were observed, leading to the failure of the reconstruction [30,31]. Therefore, an ideal functional scaffold for ligament reconstruction should have a retreat rate that mechanically and spatially matches the regeneration process.

Inspired by the physiological stages of the ligament healing process, we designed an innovative scaffold that matches the regeneration process, having dynamic mechanical properties and spatial adaptability for collagen infiltration and remolding. To customize the dynamic mechanical properties and spatial adaptability, we manipulated the trajectory of PPDO, PGCL, and PGLA in the core-shell braided structures. The braided scaffold exhibited tri-phasic mechanical behavior and excellent strength and stiffness. In this scaffold, the porosity increased from day 6 and remained stable on day 24 with the degradation of PGLA and PGCL, which was consistent with the cell proliferation and matrix deposition phase in the healing process. The scaffold exhibited good biocompatibility and promoted the adhesion and proliferation of rat tendon stem/progenitor cells (rTSPCs). *In vivo*, the regeneration process-matching scaffold promoted collagen infiltration and maintained structural integrity and sufficient strength for daily activities at 16 weeks. This regeneration process-matching scaffold with dynamic mechanical properties and spatial adaptability may be proposed as a feasible substitute to facilitate the reconstruction of ligaments.

## 2. Materials and methods

### 2.1. Materials

PPDO monofilaments (81 tex, d = 0.31 ± 0.001 mm, $M_w$ = 57.58 kg/mol), PGCL monofilaments (81 tex, d = 0.31 ± 0.001 mm, $M_w$ = 56.38 kg/mol), and PGLA multifilaments (81 tex/12 f, d = 0.33 ± 0.001 mm, $M_w$ = 62.09 kg/mol) were manufactured by a melt spinning method in Donghua University (tex: gram/1000 m, f: number of filaments). Dulbecco's Modified Eagle's Medium (DMEM), fetal bovine serum (FBS), penicillin/streptomycin (P/S), and 3-(4,5-dimethylthiazol-2-yl)-2,5-diphenyltetrazolium bromide (MTT) were purchased from Shanghai Limin Industrial Co., 100 Ltd. (Shanghai, China). Water used in the study was purified using a Milli-Q Plus 185 water-purification system (Millipore, Bedford, MA, USA) with a resistivity higher than 18.2 MΩ cm.

### 2.2. Fabrication of the scaffold

The scaffold was prepared with a 12-bobbin braiding machine (Fig. 1) (manufactured by Donghua University, China). To simulate the core-shell structure of native ligaments, composed of crimped collagen fiber bundles wrapped by synovium, we developed three braided structures with the same total number of yarns. (1) 1S3B: 3 braided bundles (12X) wrapped by 1 shell layer (12X), (2) 1S6B: 6 braided bundles (6X) wrapped by 1 shell layer (12X), (3) 2S2B: 2 braided bundles (12X) wrapped by 2 shell layers (12X). (12X: 12-yarns braided structure; 6X: 6-yarns braided structure). To further customize the degradation performance of the scaffold and optimize the internal spatial distribution and structural stability, we designed two material ratios, C1 and C2, with 6:4:2 and 4:6:2 yarn number ratios of PPDO, PGCL, and PGLA, respectively (Fig. S1, S2). The as-made scaffolds were freeze-dried after cleaning and sterilized by ethylene oxide to minimize contamination.

### 2.3. Surface morphology and porosity

The scaffold morphology was examined by a stereomicroscope (SMZ745T, Shanghai Nikon Instrument Co., Ltd.). Diameters and braiding angles were measured by MB-Ruler software (n = 6 for each group). The 3-D structure of the scaffold was assessed by an X-ray microscope (XRM; Xradia 520 Versa, Zeiss, Germany) (n = 3 for each group). The scanning energy was 80.00 kV/7.00 W, and the exposure time was 1 s. Image stacks of about 1000 virtual slices with 7.07 μm voxel sizes were acquired on XRM. XRM3DViewer and Dragonfly software was employed for 3D image processing [32].

The porosity was calculated using Equation (1) (n = 6 for each group).

$$Porosity = \frac{V_1 - (V_3 - V_2)}{V_1} \times 100\% \quad (1)$$

where $V_1$ is the theoretical volume of the sample, $V_2$ is the volume of the solution, and $V_3$ is the total volume of the sample and solution.

### 2.4. Thermal and chemical testing

Crystallinity was evaluated by an X-ray diffractometer (XRD, D/Max-2550 PC, Japan) using Cu Kα radiation (λ = 154 p.m.) over the range from 3 to 90° 2θ with a rate of 2°/min. (n = 6 for each group). Differential scanning calorimetry (DSC4000, PerkinElmer, Shelton, CT, USA) was employed to investigate the melting temperature ($T_m$) of PPDO, PGCL, and PGLA yarns (n = 6 for each group). The samples were cut into 5 mg pieces and sealed in aluminum pans. PPDO was subjected to a

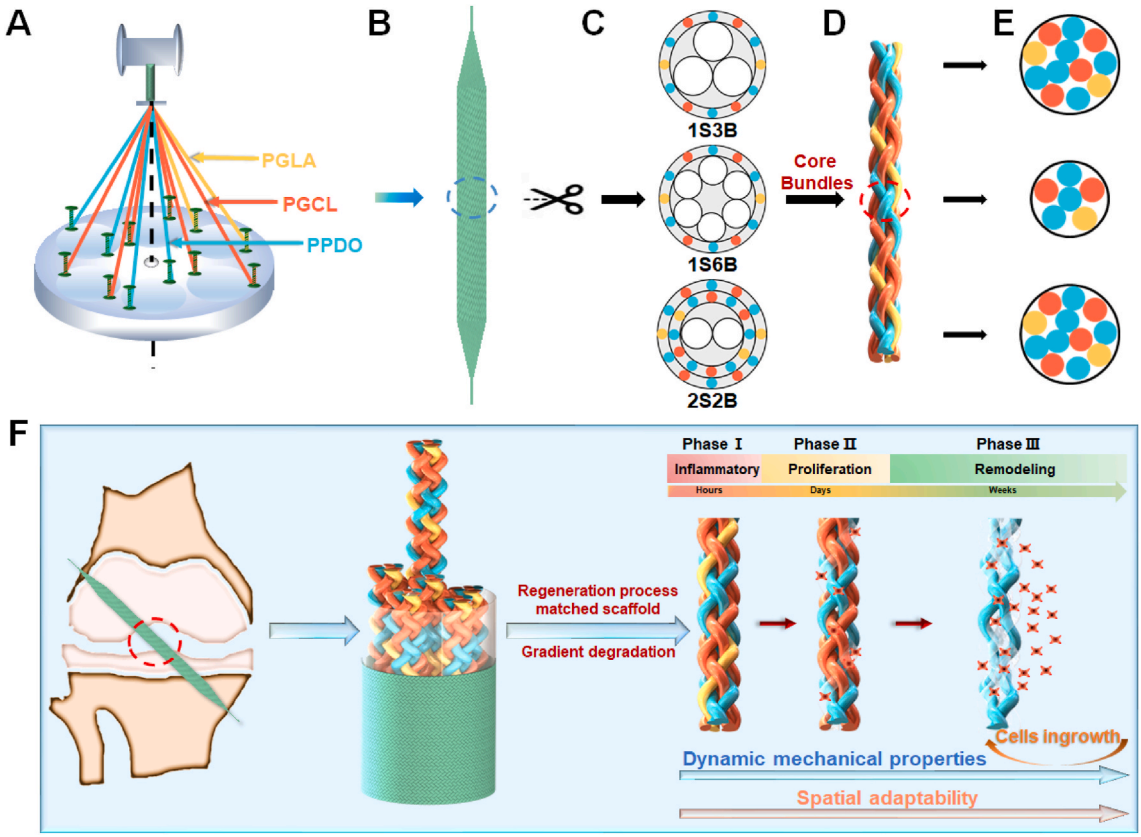


**Fig. 1.** Design and preparation schematic of scaffolds. (A) 12-bobbin braiding machine. (B) Braiding scaffolds. (C) Cross-section diagram of core-shell braided structure. (D) Core bundles. (E) Cross-section diagram of core bundles. (F) Scaffolds degrade gradient to fit the regeneration process and promote reconstruction. ● - PPDO, ● - PGCL, ● - PGLA.

heating-cooling-heating cycle from 40 to 140 °C at a rate of 10 °C/min under a nitrogen atmosphere, and PGCL and PGLA were subjected to a heating-cooling-heating cycle from 80 to 250 °C. Furthermore, the thermal stability of the three yarns was determined by thermogravimetric analysis (TGA, TA Instruments SDTQ600, USA) (n = 6 for each group). 5 mg of each sample were heated from 30 to 600 °C at a rate of 20 °C/min under a nitrogen atmosphere. The TGA curves were obtained, and the corresponding differential thermogravimetric (DTG) plots were calculated as the first derivatives of the TGA curves.

### 2.5. Mechanical testing

**Uniaxial tensile testing of yarns**: The uniaxial tensile properties of PPDO, PGCL, and PGLA yarns were determined using a YG (B) 026G-500 universal testing system instrument (Wenzhou Darong Textile Instrument Co., Ltd., China). To determine the ultimate tensile strength (UTS), stiffness, and modulus of the yarns, we conducted uniaxial tensile testing with a gauge length of 20 mm at a loading speed of 20%/sec strain rate (240 mm/min). Stiffness was measured by calculating the linear slope of the load-elongation curve between 3 and 7 mm of elongation (n = 6 per group).

**Uniaxial tensile testing of scaffolds**: It was reported that preconditioning could increase stiffness, reduce residual deformation, and stabilize the load-strain curve [33]. In this research, the samples were preconditioned with 10 cycles and cyclically extended between 1 and 5% strain with a gauge length of 20 mm at a strain rate of 10%/sec [34]. Uniaxial tensile testing was conducted with a gauge length of 20 mm at a loading speed of 20%/sec strain rate to determine scaffold load-elongation curve, UTS, and stiffness. Ligament ruptures and injuries occur quickly, at fast rates; thus, a 20%/sec strain rate was selected [34]. The stiffness was measured by calculating the linear slope of the load-elongation curve between 3 and 7 mm of elongation [2] (n = 6 per group). The apparent stress was calculated by dividing the force by the cross-sectional area measured before the test, and the net stress was determined by dividing the apparent stresses by the volume fraction ($v$) of the specimens according to Equation (2).

$$net\ \ stress = \frac{apparent\ \ stress}{v} \tag{2}$$

where $v = 1\text{-}P$, $P$ is the porosity of scaffolds.

**Cyclic tensile testing of scaffolds**: Cyclic testing was conducted with a 5% constant elongation of the 2 mm gauge length at a 2%/sec strain rate [35] for 500 cycles. A 5% constant strain level was selected because more than 6% strain levels had been suggested to cause the failure of a single collagen bundle, resulting in permanent changes in the tensile behavior of ligaments [36,37]. The peak loads during the cyclic testing were recorded every 50 cycles. The peak load decrease rate (PLR) was calculated [38] (n = 3 per group).

$$PLR = \frac{PL_{500} - PL_1}{PL_1} \times 100\% \tag{3}$$

where $PL_{500}$ is the peak load after 500 cycles and $PL_1$ is the peak load at the 1st cycle.

**Elastic recovery testing of scaffolds**: Loading-unloading testing was conducted under a 500 N loading force, which is close but does not exceed the UTS of beagle native ligaments [39,40], with a 20%/sec strain rate [34] to estimate the elastic recovery properties of prostheses under a traumatic force. The elastic recovery rate (ER) was calculated according to Equation (4) [34] (n = 3 per group).

$$ER = \frac{E_t - E_r}{E_t} \times 100\% \tag{4}$$

where $E_t$ is the total elongation and $E_r$ is the residual elongation.

**Stress relaxation testing of scaffolds**: The stress relaxation performance of scaffolds was evaluated under a fixed 5% elongation at a 2%/sec strain rate [35,37], followed by a 2100 s relaxation period. 5 peak force data were collected every 100 s. The stress relaxation rate (SR) was calculated using Equation (5) [35] (n = 3 per group).

$$SR = \frac{F_{2100}}{F_{max}} \times 100\% \quad (5)$$

where $F_{2100}$ is the force at 2100 s relaxation, and $F_{\max}$ is the maximum stress at 5% elongation.

### 2.6. Accelerated degradation in vitro

All scaffolds were cut into 5.5 cm samples5, freeze-dried after cleaning, and sterilized with ethylene oxide for 24 h. Degradation was performed by immersing scaffolds in a phosphate-buffered saline solution (PBS). The ratio of the PBS volume (mL) to the sample mass (g) was 30:1. The centrifuge tubes were placed in a shaker with a constant speed of 60 r/min at 50 °C, and the liquid was changed every 2 days. PPDO, PGCL, and PGLA scaffolds (expressed as $C_{PPDO}$, $C_{PGCL}$, and $C_{PGLA}$, respectively) with the same braided structure were used as controls. 6 samples were used for each test at each time point.

**Morphological changes**: The morphological changes of scaffolds were characterized on days 0, 6, 12, 18, 24, 30, and 36. The samples were taken out and freeze-dried. The surface morphology was observed using a scanning electron microscope (SEM; Hitachi S-4800, Japan).

**Porosity and mass loss**: The porosity was measured according to Equation (1) in section *2.3*. The mass loss was calculated using Equation (6) [41].

$$Mass\ \ loss = \frac{W_0 - W_t}{W_0} \times 100\% \quad (6)$$

where $W_t$ is the dry weight of the sample after a certain degradation period, and $W_0$ is the initial dry weight of the sample.

pH **testing of the degradation solution**: The degradation solution was collected every 2 days, and its pH value was determined by a pH meter (PHSJ-4A, Leici, China).

**Weight-average molecular weight ($M_w$) and uniaxial tensile testing**: The molecular weight was characterized by gel permeation chromatography (GPC; EcoSEC HLC-8320GPC, Japan). The tensile properties of scaffolds were characterized according to section *2.5*.

### 2.7. Cytocompatibility in vitro

rTSPCs isolated following the methods of Yanming et al. [42] were cultured in a tenocyte growth medium (TGM) containing a DMEM medium, 20% FBS, and 1% P/S [43]. All of the cells at passages 4–6 were cultured in 5% $CO_2$ at 37 °C. All scaffolds were cut into 1.5 cm in length. Before cell seeding, coverslips and scaffolds were placed in 6-well plates with stainless-steel rings and sterilized with 75% ethanol steam for 24 h. After that, a PBS solution was used to wash out the samples three times, and TGM, capable of soaking all of the samples, was added to culture in 5% $CO_2$ at 37 °C overnight. Then, TGM was sucked out, and all scaffolds were washed out with PBS before cell seeding. Cells were seeded at a density of $1 \times 10^5$ cells per fibrous scaffold for 1, 2, 4, and 8 h for cell adhesion assay and 1, 4, and 7 days for cell proliferation assay. Coverslips without scaffolds were used as controls, with the medium being replaced every 2 days. The viability and morphology of rTSPCs attached on different scaffolds were separately investigated via MTT assay and fluorescein isothiocyanate-conjugated phalloidin (green) staining. After 1, 2, 4, and 8 h of culturing, TGM was sucked out, and all scaffolds were washed out twice with PBS. A 10% MTT working solution was added to each well and cultured in a $CO_2$ incubator for 4 h. The absorbance was measured at a wavelength of 492 nm. After 1, 4, and 7 days of culturing, the seeded cells gradient dehydrated in 30–100% ethanol were fixed with 4% paraformaldehyde, and then fluorescein isothiocyanate-conjugated phalloidin (Invitrogen, USA) was employed. A TS100 fluorescence microscope (Nikon, Japan) was used to examine cell proliferation (n = 3 per group and time point).

### 2.8. Subcutaneous implantation and histological evaluation

All scaffolds cut into 1.5 cm in length and sterilized by ethylene oxide were subcutaneously implanted in six-week-old male rats (weighing approximately 200–250 g, purchased from Shanghai Jiesijie Laboratory Animal Co., Ltd, Shanghai, China). PET scaffolds with the same braided structure were set as controls. The experimental samples were implanted symmetrically on one side of the back, and the PET scaffolds were embedded on the other side of the same rat. 7, 14, and 21 days post-operation, the entire subcutaneous tissue containing scaffolds was excised from euthanized animals and fixed in 4% (w/v) buffered formalin overnight (n = 6 per group and time point). The samples were paraffin-embedded and sectioned to a 300 μm thickness. Sections were stained with hematoxylin and eosin (H&E) (Gibco, USA) for evaluation of the inflammation and with Masson's Trichrome (Masson) (Gibco, USA) for observation of collagen infiltration using a light microscope (Olympus BX41, Japan) and photographed by a DP71 camera (Olympus, Japan). Semi-quantitative analyses of the inflammatory area (%) and the collagen deposited area (%) were performed using Image-Pro Plus 6.0 software (Media Cybernetics, Silver Spring, MD, USA).

### 2.9. Animal model of ligament reconstruction

**ACL reconstruction**: According to the method in section *2.2*, scaffolds that fit the size of the rabbit knee ligament, ACL, were customized. The diameter and length of the customized GDS were 2.32 ± 0.12 mm and 2.03 ± 0.38 cm, respectively, with two 10 cm long traction lines at each end (Fig. S7). The as-made scaffolds were cleaned with deionized water and sterilized by ethylene oxide. 54 rabbits were randomly divided into the GDS group and the PET group, with 9 rabbits in each group for 3-time points. Then, the knee ligament reconstruction procedure was performed according to the previous study [44,45]. Briefly, after exposing the right posterior knee joint and cutting the native ACL, tibial and femoral tunnels were established with a drill along with the original ACL footprint. Afterward, the scaffold was pulled into the tibial tunnel and passed through the femoral tunnel using a PPDO-II suture (Ethicon, Puerto Rico, USA). Both ends of the graft were sutured with the adjacent periosteum and soft tissue, and the wound was closed layer by layer. In each group, 9 rabbits were sacrificed at 4, 8 and 16 weeks postoperatively for further evaluations, including macroscopic observation (n = 9), histological and immunofluorescence assessment (n = 3), biomechanical testing (n = 6) and micro-computed tomography (CT) analysis (n = 3).

**Histological and immunofluorescence assessment**: The 4-week, 8-week, and 16-week specimens were sacrificed to evaluate the histological properties and immunofluorescence imaging (n = 3 per group and time point). These samples were decalcified at room temperature in 10% ethylenediamine tetraacetic acid for one month. Then, the samples were dehydrated, embedded in paraffin, and sectioned at a thickness of 5 μm perpendicular to the longitudinal axis of the bone tunnel. The sections were stained with H&E (Gibco, USA), Masson trichrome (Gibco, USA), and observed with inverted light microscopy (IX71SBF-2, Olympus Co., Japan). Digital images were taken using a DP Manager (Olympus Optical Co., Japan). Besides, the picrosirius red staining (PSR) (Gibco, USA) images under a polarized light microscope (Leica DM4000-B, Germany), CD3 (Thermo Fisher, USA), and CD68 (Thermo Fisher, USA) images under LSM 700 laser scanning microscope (Carl Zeiss, Germany) were obtained. Further quantitative analyses were performed using Image-Pro Plus 6.0 software (Media Cybernetics, Silver Spring, MD, USA). H&E was used to assess the intraosseous graft-to-bone

integrations by calculating the average width of the interface between bone and the graft, while Masson trichrome staining was used to analyze the collage infiltration into the scaffold [46,47]. Under polarized light microscopy, thicker type I collagen fibers appeared orange or yellow, whereas thinner type III collagen fibers were green. The PSR images were used to further analyze collagen deposition and maturation using Adobe Photoshop CC (Photoshop CC, Adobe Systems Inc., USA) and Image-Pro Plus 6.0 (Media Cybernetics, Silver Spring, MD, USA) software by color factor [48,49]. CD3 (in orange) and CD68 (in red) staining were used to identify immune cells.

**Micro-CT**: The remaining 16-week specimens post-operation of both groups were scanned using a Skyscan 1176 micro-CT imaging system (Bruker, Kontich, Belgium) to analyze the graft osseointegration process in the bone tunnel at a spatial resolution of 35 μm (1 mm aluminum filter, 65 KV, 380 μA). The images were reconstructed and evaluated using customized software (DataViewer, CTvol and CTAn) [44,50]. The average cross-sectional bone tunnel area ($mm^2$) was measured from femoral and tibial tunnels, and the 3D-reconstructed datasets were used to calculate the trabecular bone volume fraction of the total tissue volume (BV/TV, %) within the region of interest.

**Biomechanical test**: At 4, 8, and 16 weeks, 36 rabbits (n = 6 per group and time point) used for biomechanical tests were sacrificed to obtain knee samples. Then, the samples were carefully dissected to remove soft tissue around the graft, and the femur-graft-tibia complexes (FGTCs) were subsequently fixed on the mechanical testing with a universal electronic material testing machine (AGS-X, Shimadzu, Co., Japan). After preloading, a 5 mm/min load-displacement rate was applied to the samples until the graft was pulled out of the bone tunnel or ruptured. The ultimate failure load and stiffness were noted according to the load-deformation curve [44,45].

### 2.10. Ethics statement

The used experimental animal protocols were strictly according to the Institutional Animal Care and Use Committee (IACUC) policy of Shanghai Jiao Tong University Affiliated Sixth People's Hospital. The IACUC has approved this study. Ethical principles were followed throughout all experimental procedures. All animal experiments were performed according to the Animal Management Regulations of China (1988 and revised in 2017, Ministry of Science and Technology).

### 2.11. Statistical analysis

The data were analyzed by SPSS version 26 for Windows (SPSS Inc., Chicago, IL, USA). All results were expressed as mean ± standard deviation (SD). The significance between the data groups was tested using the One-way ANOVA test. A value of $p < 0.05$ was considered significant and indicated with (*), $p < 0.01$ was indicated with (**), and $p < 0.001$ was indicated with (***).

## 3. Results and discussion

### 3.1. Fabrication and characterization of the scaffolds

Inspired by the remarkable tri-phasic mechanical properties and excellent axial tensile strength resulting from the crimped collagen fiber bundles wrapped by synovium, we designed a braided structure in which a shell wrapped core bundles. Three braided structures, 1S3B, 1S6B, and 2S2B, were developed to customize the mechanical properties (Fig. 1C). (1) 1S3B: 3 braided bundles (12X) wrapped by 1 shell layer (12X), (2) 1S6B: 6 braided bundles (6X) wrapped by 1 shell layer (12X), and (3) 2S2B: 2 braided bundles (12X) wrapped by 2 shell layers (12X). (12X: 12-yarns braided structure). We designed two material ratios to further optimize the degradation performance and spatial adaptability to fit the regeneration process (C1 and C2 with 6:4:2 and 4:6:2 yarn number ratios of PPDO, PGCL, and PGLA, respectively) (Fig. S1, S2).

The morphology of the prepared scaffolds is shown in Fig. 2. PPDO, PGCL, and PGLA are uniformly distributed in the shell layers and core bundles of six scaffolds. The trajectory position of PPDO, PGCL, and PGLA is transferred along the axial direction of the scaffold (Fig. 2C; Videos S1 and S2, Supporting Information). The average diameter of all scaffolds is 3.71–4.41 mm as designed, similar to the beagle ACL diameter. The braiding angles of core bundles and shell layers are 19.27–30.05° and 33.85–40.81° (Table S1), respectively. It was reported that the crimped angle of the collagen fiber bundles in native ligaments is 15–45° [6], so the synthesized scaffold successfully replicates the crimped angles of native ACL. In particular, the 1S6B structure exhibits a minimum braiding angle, and there is no obvious difference between C1 and C2. This is because the core bundles of 1S6B are diamond-braided structures with the yarns intertwining one up and one down, leading to a stronger orientation of yarns along the axial direction of the scaffold. As shown in Fig. 2D, the initial porosity of scaffolds is 35.43–53.74%, which can provide sites for early cell adhesion. In the early stage of implantation, the main function of the scaffold is to bear the load and avoid graft fracture.

Supplementary data related to this article can be found at https://doi.org/10.1016/j.bioactmat.2021.11.001.

### 3.2. Thermal and chemical properties

The XRD analysis of PPDO, PGCL, and PGLA yarns was performed to study the crystalline structure, and the results are shown in Fig. 2E. PPDO exhibits a 56.04 ± 8.00% crystallinity with two characteristic peaks at 21.82° and 23.50°, confirming the semi-crystalline structures. PGCL shows two characteristic peaks at 21.78° and 28.52° (60.85 ± 2.76%), while PGLA possesses two characteristic peaks at 21.60° and 28.44° (52.71 ± 5.10%) [51]. DSC and TGA measurements were performed to evaluate the thermal properties of PPDO, PGCL, and PGLA. Fig. 2F shows the DSC curves, indicating the melting behavior of the samples. The $T_m$ values of PPDO, PGCL, and PGLA are 104.85, 197.22, and 194.33 °C, respectively. The thermal degradation properties are presented in Fig. 2G and H. The maximum thermogravimetric rates of PPDO, PGCL, and PGLA occur at 339.44, 418.95, and 374.92 °C, respectively. The above results demonstrate that the three yarns have good thermal stability.

### 3.3. Mechanical properties of the scaffolds

Most failures related to synthetic grafts occur due to the mismatch of mechanical properties, so the mechanical properties of the scaffold are crucial for ACL reconstruction.

Tri-phasic mechanical properties originating from the crimped collagen fibers are at the core of the mechanical performance of ACL. Sufficient tensile strength and appropriate stiffness are necessary to maintain the stability of the joint. The mechanical properties of the three prepared yarn materials are shown in Fig. 3A–C and Fig. S3A, 3B. As can be seen from Fig. 3D and Fig. S3C, the obtained scaffolds possess tri-phasic mechanical properties. In the initial stretching stage, the yarns tend to straighten in the axial direction, and the braiding angle decreases, which is manifested as the "toe region". As the load increases, the molecular chain of the yarn becomes oriented, and the stress-strain and load-elongation curves show linear behavior. The slopes of the stress-strain and load-elongation curves determine the tensile modulus and stiffness, respectively. Finally, the yarns break at the ultimate load. The UTS and stiffness are shown in Fig. 3E and F. The UTS of the scaffolds is 75.04 ± 2.90–109.66 ± 3.04 MPa and is higher than beagle natural ACL (38.04 ± 2.67 MPa) [39]. For all braided scaffolds, the net stress is 2 times higher than the apparent ones (Fig. S3E). The stiffness is 67.40 ± 1.66–92.60 ± 4.83 N/mm, similar to natural beagle ACL (74.30 ± 7.00 N/mm) [39]. The Young's modulus (Fig. S3D) is within the value range of natural ligaments [27]. The stress and energy to yield/failure point (Table S2) are higher than those of the natural ligaments [2,36].

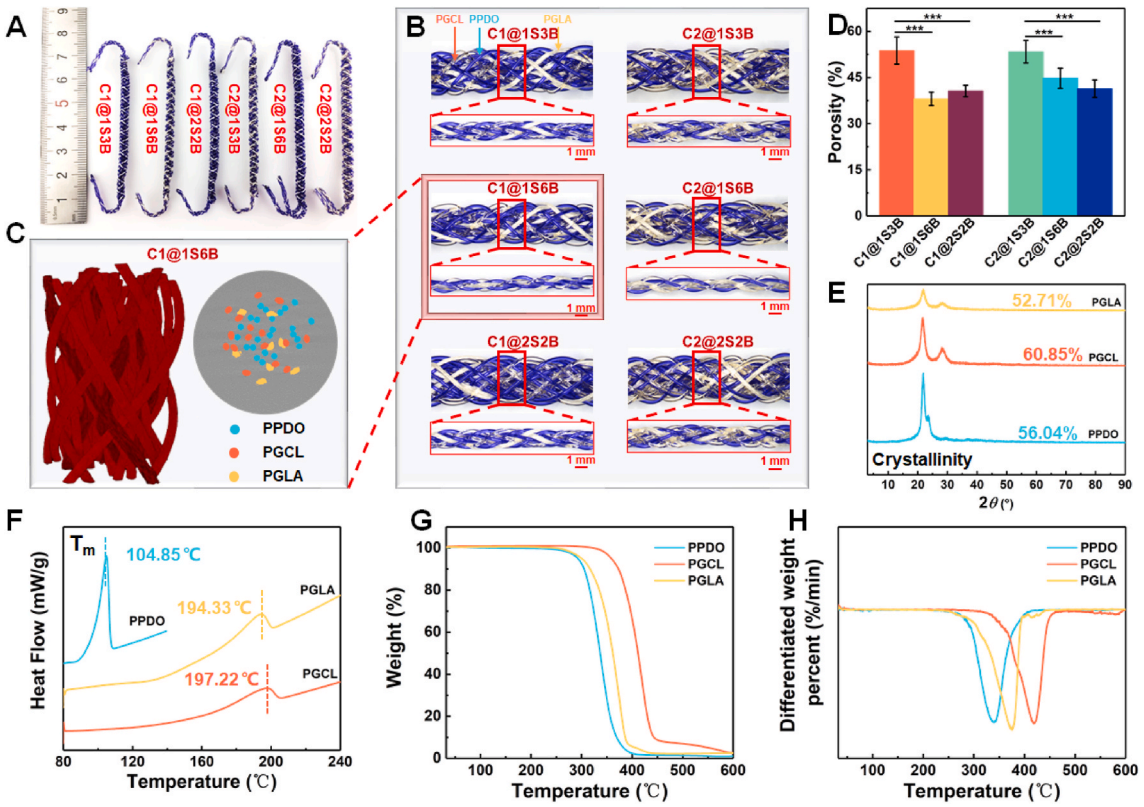


**Fig. 2.** (A) Digital photos of six scaffolds. (B) Core and shell morphology of six scaffolds. (C) XRM images of the 3-D structure and cross-section of C1@1S6B. (D) The porosity of six scaffolds. (E) XRD, (F) DSC, (G) TGA and (H) DTG diagrams of PPDO, PGCL and PGLA yarns.

Disappointingly, the strain to failure point (95.28–122.61%) exceeds that of the natural ligaments (50.90–61.00%) [26,36], which is caused by the elongation of the braided structure during stretching. 1S6B exhibits the highest UTS, stiffness, and modulus for the three braided structures, while 2S2B shows the lowest values. More core bundles yield greater friction and holding force, providing better mechanical properties. As the 2S2B structure demonstrates the worst mechanical response, 1S3B and 1S6B structures are selected for subsequent fatigue tests.

Since ligaments are normally stretched back and forth during their service life, the cyclic tensile properties of the scaffolds also need to be tested. The results of cyclic tensile are shown in Fig. 3G and J. A 13–18% decrease of the maximum load after 500 cycles with a 5% constant elongation is observed for all groups. C1@1S6B and C2@1S6B exhibit a lower decrease rate. The smallest braiding angles of the 1S6B structure limit the yarn elongation range when subjected to cyclic tension [52]. The peak load decrease rate of the scaffold is lower than that of ligament prosthesis (17–29%) [40], indicating suitable fatigue resistance properties when used *in vivo*.

The failure of ligament reconstruction often occurs due to the lack of prosthesis elasticity [41]. It is significant for the joint's stability that prostheses can quickly recover to their original position after stretching. As shown in Fig. 3H and K, when the load is close to the UTS of native ACL, the scaffolds can still recover to more than 60% of their original length. The strain recovery ability of the scaffold is better than that of the braiding ligament prosthesis (30–59%) [34,53].

Stress relaxation of prostheses caused by cumulative damage *in vivo* was reported to be one of the reasons for the reconstruction failure [36]. Therefore, the scaffolds need to have resistance to stress relaxation. As shown in Fig. 3I, L, the results of 30 min of stress relaxation show that the force required to maintain the daily elongation (5% strain) of the scaffold is 40–50% of the initial stress, which may indicate a scaffold elongation caused by the slippage of the braided bundles during stretching.

It can be seen from the above that the obtained scaffold exhibits triphasic mechanical properties, excellent UTS, and stiffness. Fatigue resistance shows that the scaffold can maintain the relative positions of the femur and tibia and avoid early fatigue failure after reconstruction. The 1S6B structure shows good mechanical properties, without a significant difference between C1 and C2. To further verify the degradation performance between C1 and C2, C1@1S6B and C2@1S6B are selected for the accelerated degradation tests *in vitro*.

### 3.4. Evaluation of accelerated degradation in vitro

To evaluate the degradation performance of the scaffold, we performed an *in vitro* accelerated degradation experiment at 50 °C to simulate the degradation process rapidly. Theoretically, the degradation of PPDO, PGCL, and PGLA typically follows a bulk erosion mechanism through the hydrolysis of ester bonds [54]. In the initial stage of degradation, the interchain ester bonds break with the rapid water diffusion into the amorphous region of the polymer, and the insoluble macromolecular chains are gradually sheared into small soluble molecules and finally decomposed into water and carbon dioxide through the hydrolysis reaction and discharged through metabolism. With the degradation process, water gradually permeates from the amorphous to the crystalline region, causing the molecular chains in the crystalline region to undergo a hydrolysis reaction and disintegrate [41]. During accelerated degradation at 50 °C, no phase transition occurs in the polymer material (Table S3). The scaffold exhibits a gradient degradation behavior due to the sequential degradation of PGLA, PGCL, and PPDO fibers. Therefore, in the following, scaffolds with the 1S6B braided structure are named gradient degradation scaffolds (GDS).

The structure and morphology of the scaffolds change progressively during 0–36 days, as shown in Fig. 4A and B, and Fig. S4-S6. For C1@GDS and C2@GDS, there is no apparent change on day 6. On day 12, the PGLA multifilaments in C1@GDS and C2@GDS exhibit a

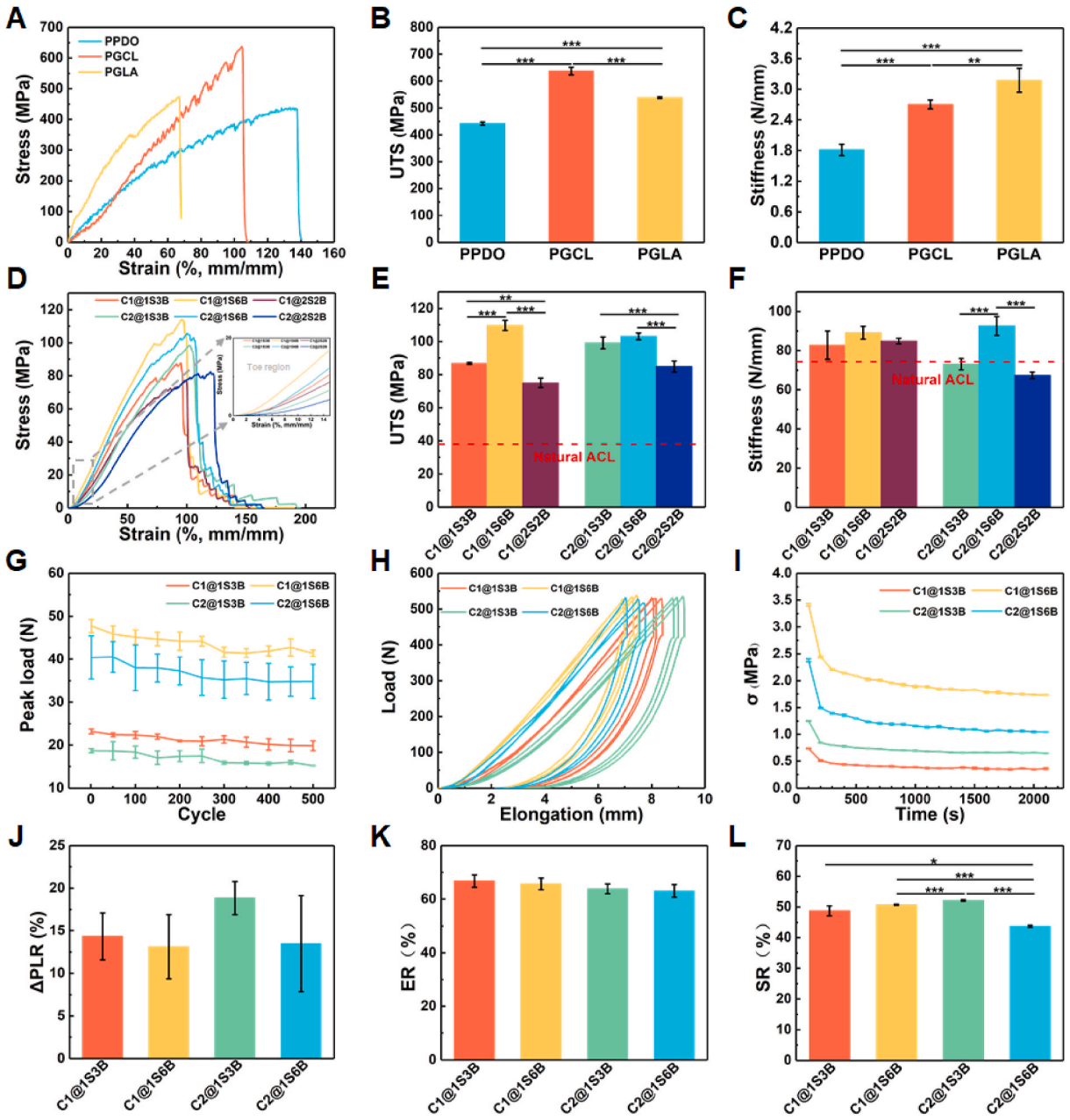


**Fig. 3.** Mechanical properties. (A) Tri-phasic mechanical properties, (B) UTS, and (C) Stiffness of PPDO, PGCL, and PGLA yarns. (D) Tri-phasic mechanical properties, (E) UTS, and (F) Stiffness of scaffolds. (G) Peak load changes during 500 cycles. (H) Loading-unloading cyclic curves. (I) Stress-relaxation curves. (J) Peak load attenuation rate (PLR) during 500 cycles. (K) Elastic recovery rate (ER). (L) Stress relaxation rate (SR).

transverse fracture phenomenon. The PGCL monofilaments in C1@GDS and C2@GDS show longitudinal splitting. On day 18, the degradation of PGLA and PGCL in C1@GDS and C2@GDS is enhanced (Fig. S5). Meanwhile, the structures of $C_{PGCL}$ and $C_{PGLA}$ collapse and break into fragments (Fig. S6) and cannot be collected further. Over time, the PGLA and PGCL degradation fragments are discharged from the scaffolds during days 18–30, while PPDO retains an intact braided structure. On day 36, PGLA and PGCL in C1@GDS and C2@GDS entirely fall off, leaving a visible space, the PPDO components with a few cracks on the surface still maintain the skeleton, while $C_{PPDO}$ only cracks on the surface of the PPDO monofilament and shows a tight braided structure (Fig. S6).

As shown in Fig. 4C, the mechanical loss time for C1@GDS and C2@GDS is 30 days. The mechanical loss rate of C2@GDS at 6 days is faster than that of C1@GDS due to its lower PPDO content and high PGCL content. After 6 days of degradation, water diffuses into the amorphous region of the polymer (Fig. 4E), breaking the interchain ester bonds, so the degradation fragments start to fall off from the scaffold, as evidenced by the mass loss curve (Fig. 4F), causing a gradual increase of porosity (Fig. 4D). At 12 days, PGLA and PGCL in C1@GDS and C2@GDS begin to produce degradation fragments, and the mechanical properties decrease further. In the meantime, the internal space of the scaffold gradually increases, which is conducive to collagen deposition. At 24 days, with the degradation of PGLA and PGCL, the mass-loss rates of C1@GDS and C2@GDS are 31.60% and 41.13% (Fig. 4F), respectively, yielding a porosity of 81.40% and 85.93%, (Fig. 4D), and meeting the requirement of 70% porosity for tissue regeneration [26,55]. From 24 days to 36 days, although the mass loss rate of C1@GDS and C2@GDS further increases to 48% and 53% (Fig. 4F), respectively, the porosity does not increase significantly. This may be because most PGLA and

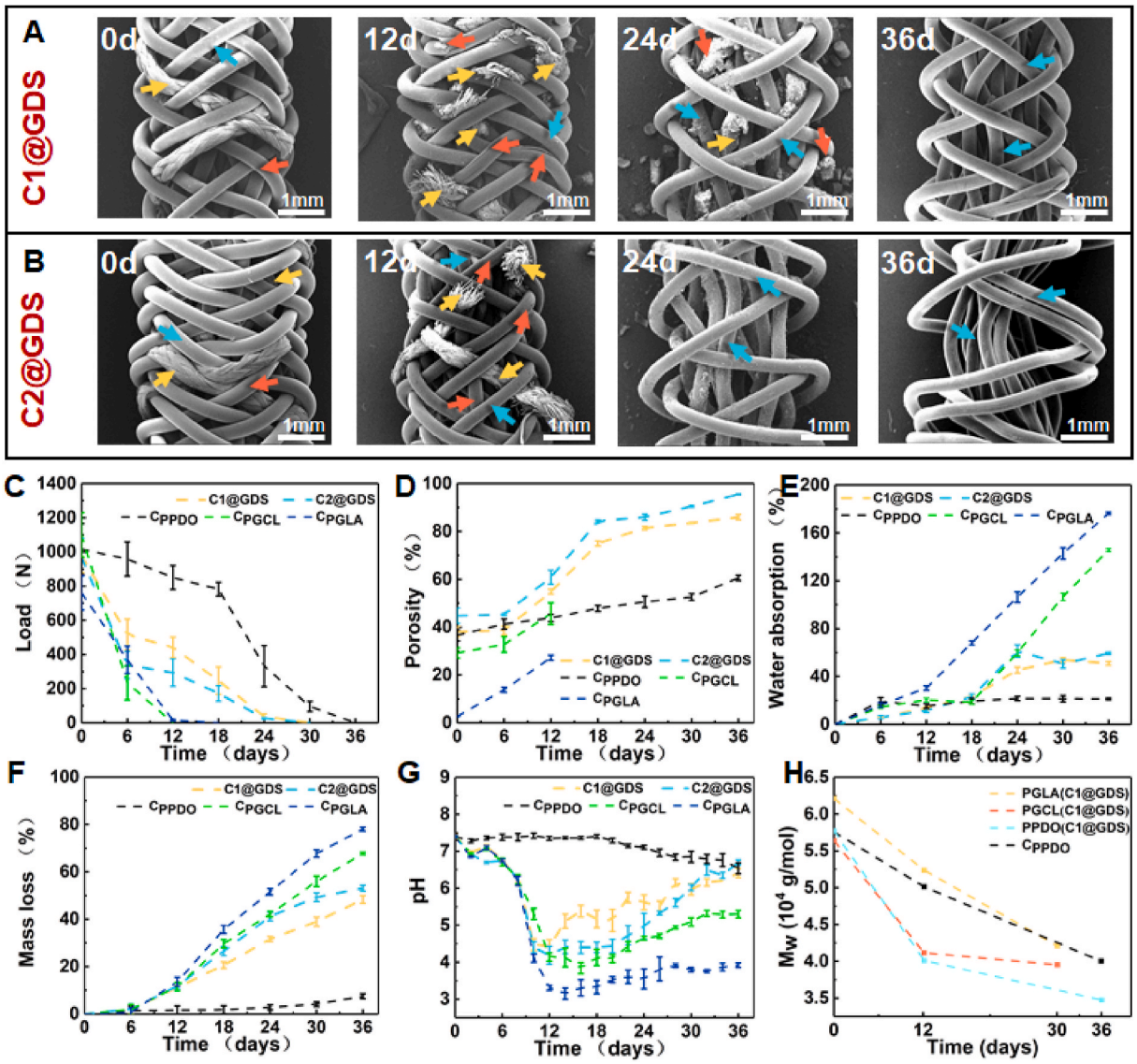


**Fig. 4.** SEM images of (A) C1@GDS, (B) C2@GDS, (C) Mechanical property, (D) Porosity, (E) Water absorption, (F) Mass loss, (G) pH, and (H) Weight-average molecular weight changes during degradation in PBS buffer at 50 °C. The yellow, red, and blue arrows indicate PGLA, PGCL, and PPDO, respectively.

PGCL are fractured and degraded into fragments at 24 days, leading to an increase in the internal space of the scaffold, but there may be a delay in the removal of degradation debris from the scaffold [26]. Based on the application environment of ACL *in vivo* and the structural variability under the force of the scaffold, this phenomenon may be alleviated *in vivo*. In addition, it can be seen that the early collapse of $C_{PGLA}$ and $C_{PGCL}$ cannot provide the structural integrity required for cell growth. On the contrary, $C_{PPDO}$ maintains a tight braided structure with limited space (60.57% porosity) for tissue ingrowth on day 36 (Fig. S6). The changes in the pH value of the degradation solution (Fig. 4G) and the molecular weight of the polymer (Fig. 4H) also verifiy the above process. More importantly, it can be observed that the adverse acidic environment caused by the degradation products is improved in the gradient-degradable scaffold.

In brief, the *in vitro* accelerated degradation results demonstrate that the pace of gradient degradation allows the scaffold to provide perforating channels to enable the ingrowth of autologous tissues and maintain structural integrity during the proliferation phase while retreating slowly during the remodeling phase to progressively transfer its load-bearing burden to the regenerated tissue and promote the collagen remodeling. Moreover, the adverse acidic environment caused by the accumulation release of acid degradation products is improved due to the different degradation times of the gradient-degradable scaffold.

### 3.5. Cell adhesion and proliferation

rTSPCs were seeded on C1@GDS and C2@GDS to analyze the adhesion and proliferation for 1, 2, 4, 8 h and 1, 4, 7 days. As shown in Fig. 5A and B, there is no significant difference in the adhesion between scaffolds and coverslips, mainly due to the disability to adjust the pore size of the soft scaffold in static culture. On day 1, there is no obvious difference between coverslips and scaffolds. However, on day 4, the cell viability significantly increases (122.84–164.03%), especially for C2@GDS (164.03%). Laser confocal images (Fig. 5C) illustrate that the spread area and size of rTSPCs on C1@GDS are large, having a spindle shape, whereas, on C2@GDS, rTSPCs are small and have no obvious pseudopodia with an ellipsoid shape [56,57]. After 4 and 7 days of culturing, a higher cell viability of rTSPCs is observed in the GDS than in the coverslips, indicating that the 3-D structure of the scaffold provides more space for cell proliferation. When cultured for 7 days, the cell viability of C1@GDS and C2@GDS remains 80–90%. The MTT results

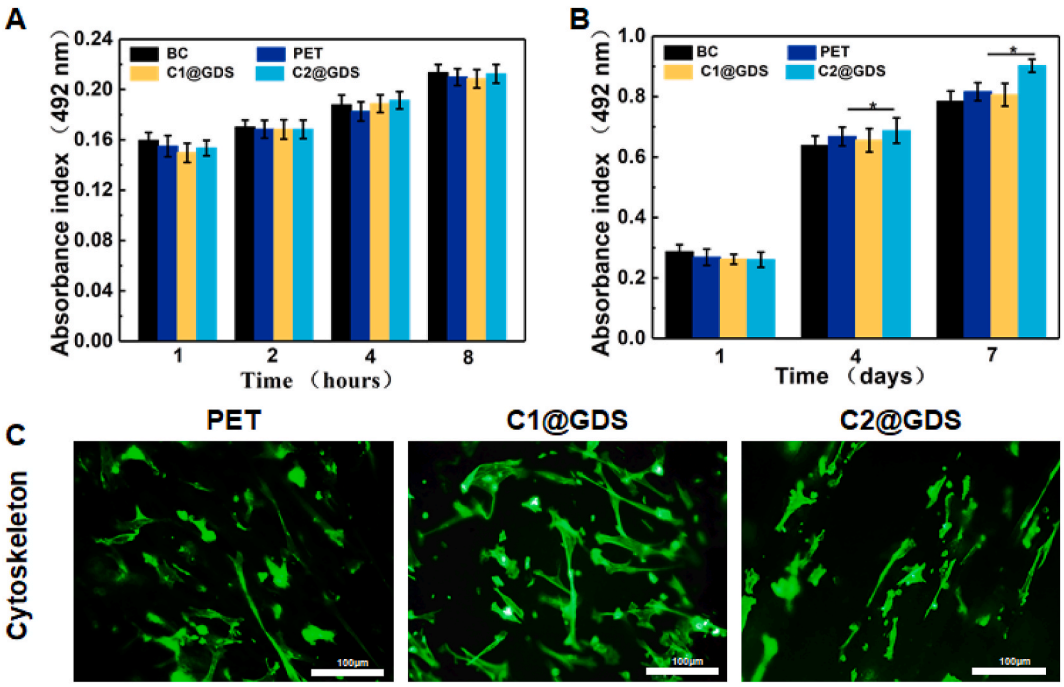


**Fig. 5.** Adhesion viability and proliferation viability of rTSPCs cultured with coverslip, PET, C1@GDS, and C2@GDS for (A) 8 h and (B) 7 days via MTT assay. (C) Fluorescein isothiocyanate-conjugated phalloidin (green) staining assay of rTSPCs on different scaffolds after culturing for 4 days.

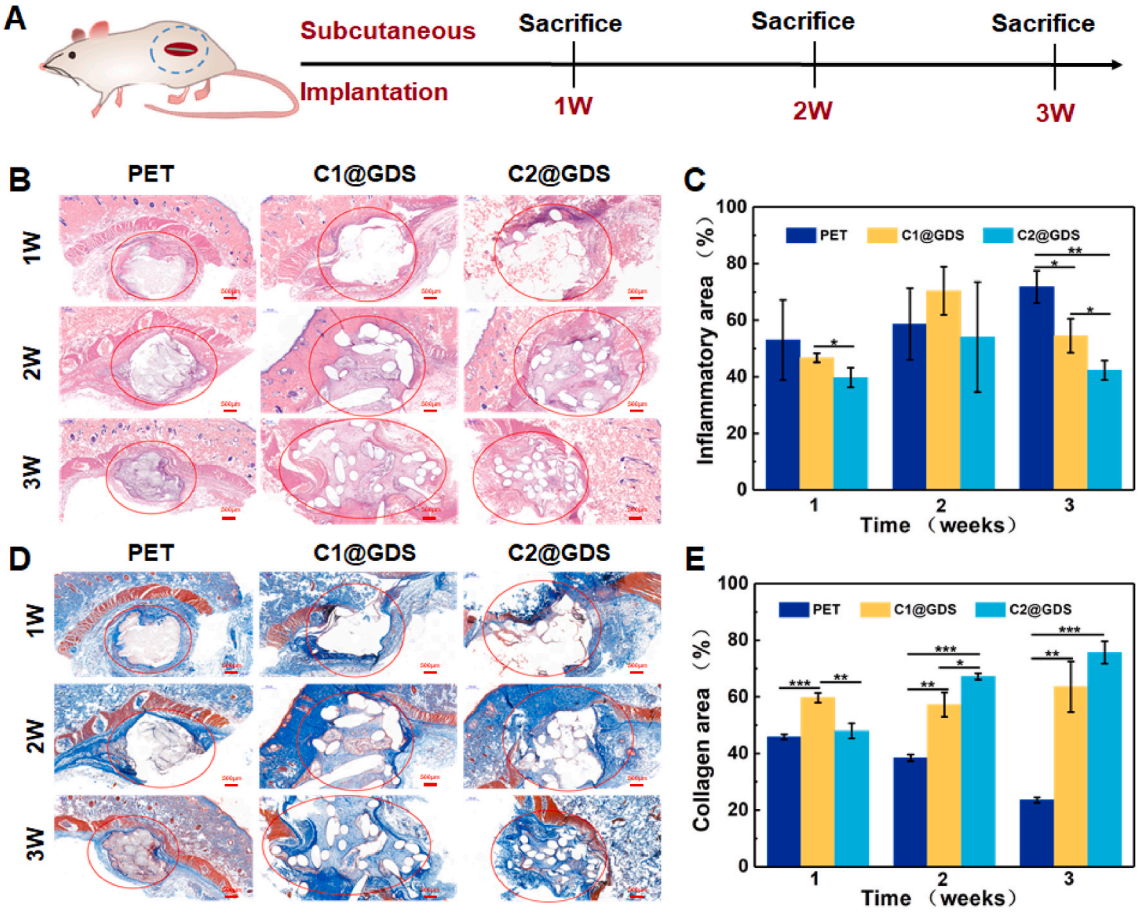


**Fig. 6.** Subcutaneous implantation in rats. (A) Experimental design for subcutaneous implantation. (B) H&E staining images, (C) Inflammatory area, (D) Masson staining images, and (E) Collagen area of PET, C1@GDS, and C2@GDS after subcutaneous embedding in rat for 21 days.

indicate that the scaffolds can enhance the cell proliferation.

### 3.6. Biodegradability and biocompatibility in vivo

Biomedical scaffolds need to have good biocompatibility. More importantly, the scaffold degradation rate should match the self-tissue regeneration process while maintaining mechanical stability and structural integrity. Therefore, we designed subcutaneous implantation experiments to verify the biocompatibility of the obtained scaffolds *in vivo*. Simultaneously, a preliminary study on the rate of scaffold degradation and tissue regeneration *in vivo* is conducted (Fig. 6A).

No rats die after subjecting to subcutaneous implantation. The immunocytes infiltration can be observed in the tissue around the scaffold after implantation by H&E staining [5,41,58,59]. The infiltration area of inflammatory cells increases at 2 weeks, caused by the degradation of PGLA and PGCL (Fig. 6B and C). After two weeks, the inflammatory cells in GDS are significantly reduced, especially in C2@GDS, probably due to the slow degradation of PGLA and PGCL and without the PPDO degradation (Fig. 4A and B). The PET group still exhibits severe inflammatory tissue infiltration at 3 weeks due to its disability of removing the scaffold material causing foreign body reaction. In addition, dense collagen fibers appear in the central area of GDS at 3 weeks, as evidenced by Masson staining (Fig. 6D and E), having only little collagen deposition in the PET scaffold. This may be because the GDS degradation provides space for the collagen matrix deposition, while the surface fibrinolysis of the PET scaffold yields a dense structure and hinders the internal infiltration of cells and collagen matrix [5,41,60].

This subcutaneous implantation demonstrates good biocompatibility of GDS. The GDS effectively alleviates the chronic inflammatory response caused by the concentrated release of acidic degradation products. More importantly, collagen fibers are found in the GDS accompanied upon material degradation, indicating the tissue induction potential of the gradient-degradable structure in ligament regeneration.

### 3.7. Ligament reconstruction evaluation

Finally, we designed a rabbit ligament reconstruction model to evaluate the tissue regeneration of GDS under stress (Fig. 7A). The gross morphology of the intraarticular graft is shown in Fig. 7B. At 4 weeks, noticeable pores appear on the surface of GDS scaffolds, caused by the degradation of PGLA and PGCL fibers, while the PET scaffolds have a dense structure. Fig. 7E demonstrates that the infiltration of macrophages (CD68) and T cells (CD3) on the interface tissues in the GDS group is lower than that of the PET group [61]. At 8 or 16 weeks, slight synovial coverage in the PET groups indicates a persistent inflammatory

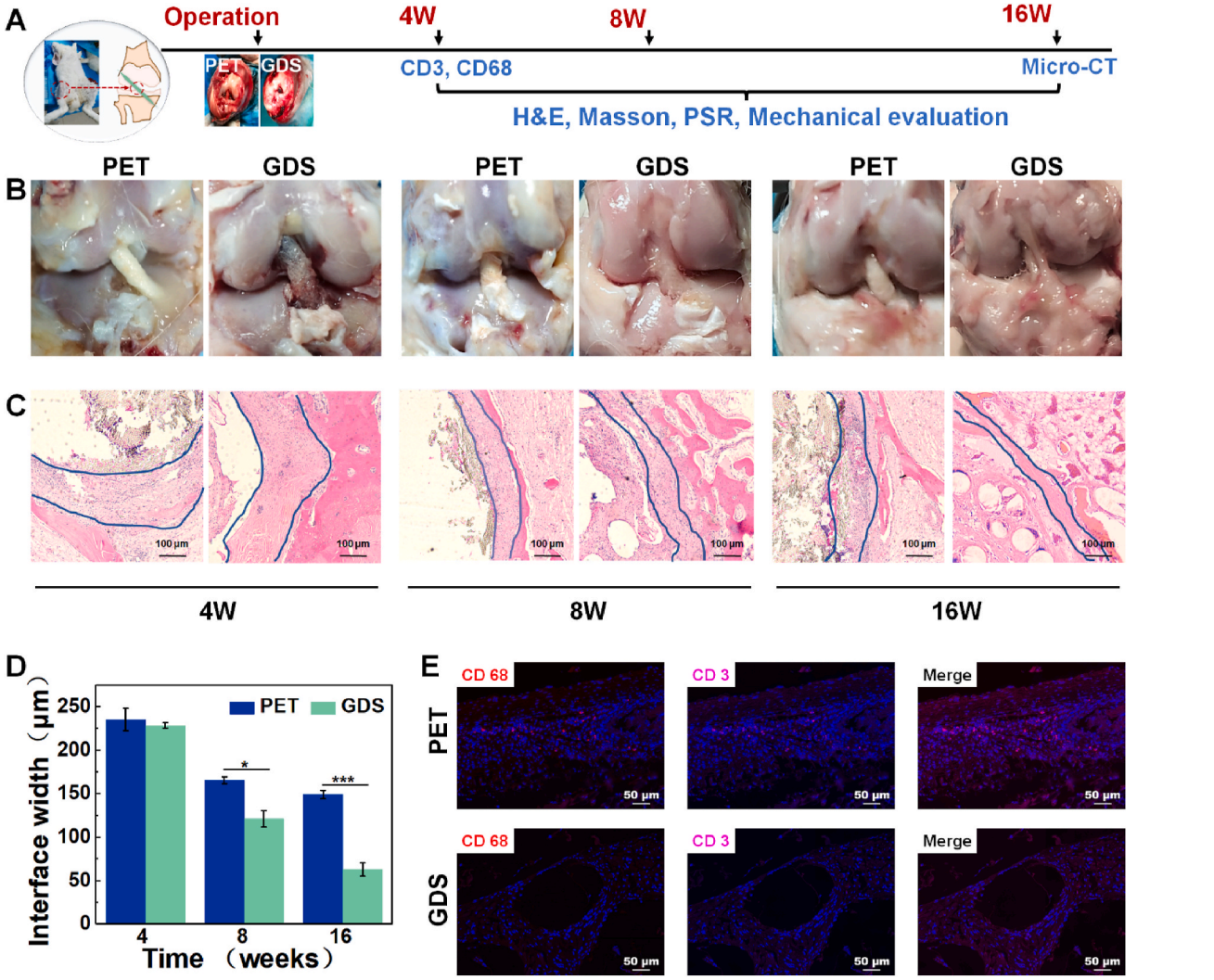


**Fig. 7.** Ligament reconstruction evaluation. (A) Schematic diagram of timeline of the ligament reconstruction. (B) Gross morphology of the regenerated ACL. (C) H&E staining images, scale = 100 μm. (D) Quantification of the interface width between the tissue and scaffold. (E) Immunofluorescence staining of CD68 (in red) and CD3 (in orange) expression in 4-week specimens, scale = 50 μm.

response, while glossy newborn tissues are observed in the GDS group. The histological analyses show better ligament-to-bone integration than the PET groups, as demonstrated by the healing interface width in H&E staining sections (Fig. 7C and D) [47,62].

Masson and PSR staining were used to evaluate collagen regeneration and remodeling. Masson staining (Fig. 8A and C) reveals a significantly higher collagen infiltration percentage in the GDS group at 8 or 16 weeks. To further quantify the subtype and maturation of collagen fibers, we analyzed the polarized light images of PSR staining. The results show that a more mature and remodeled collagen matrix forms in the GDS group, especially collagen type I. As shown in Fig. 8B, the regenerated collagen fibers exhibit a crimp morphology, and the maturity and structure are gradually improved with time, which is proved by the birefringence of collagen (Fig. 8D). At 16 weeks, the content of type I collagen is 91.35% (Fig. 8E), similar to that in natural ligaments [27]. On the contrary, the PET group exhibits a disordered arrangement and low maturity of collagen fibers caused by the compact structure and stress shielding effect. It can be seen that GDS allows the infiltration of collagen fibers and made the scaffold escape the stress shielding effect by providing dynamic mechanical properties and adjustable space.

Moreover, typical images of the cross-sectional femoral and tibial bone tunnels at 16 weeks postoperatively in Fig. 9A show more new bone ingrowth into the bone tunnel in the GDS group, indicating a superior graft osseointegration process *in vivo*. The quantitative measurements of the average bone tunnel area in Fig. 9B and BV/TV in Fig. 9C further determine that GDS can reduce the bone tunnel area and increase BV/TV, which firmly enhances the osseointegration of the ligament compared to the PET group.

As shown in Fig. 9D–G, the initial failure load, UTS, stiffness, and modulus of the scaffold are 494.98 ± 14.40 N (Native ACL: 131.82 ± 17.64 N) [63], 117.15 ± 3.41 MPa (Native ACL: 32.78 ± 4.04 MPa) [27], 42.24 ± 0.80 N/mm (Native ACL: 47.07 ± 14.84 N/mm) [63], and 199.97 ± 3.79 MPa (Native ACL: 65–111 MPa) [26], respectively. The mechanical results of FGTCs are shown in Fig. 9D–G. At three time points, all PET scaffolds are pulled out from the bone tunnel without any rupture at mid-substance due to the poor integration between bone tissue and scaffolds (n = 6 per group and time point). The failure load increases from 32.83 N at 4 weeks to 70.81 N at 16 weeks, suggesting the occurrence of tendon-bone healing. For the GDS group, the same phenomenon is observed at 4 and 8 weeks, and the failure load at 8 weeks is 76.80 N (53.48 N for PET scaffolds), indicating a better tissue integration of GDS. At 16 weeks, the mechanics of the remaining PPDO is lost, and the fracture occurs at mid-substance of the FGTCs with an 89.17 N failure load, which is 67.65% of natural rabbit ACL [63]. We analyzed the knee function of the rabbit at the final time point of 16 weeks after the scaffold is implanted (n = 9), which helps understand the functional restoration of the native ligament achieved by this scaffold (Videos S3 and S4, Supporting Information). When the rabbit is walking and running, the gait of the reconstructed knee in the GDS group is similar to that of the normal contralateral knee, and the rabbit can run. However, in the PET group, the gait of the reconstructed knee is not normal, disabling the rabbit run, which is different from the rabbit in the GDS group.

Supplementary data related to this article can be found at https://doi.org/10.1016/j.bioactmat.2021.11.001.

It can be seen from the rabbit ligament reconstruction model that GDS can promote collagen infiltration and graft-to-bone integration under stress. A synovial-like tissue is observed at 8 weeks, and sufficient mechanical properties are maintained at 16 weeks.

## 4. Conclusion

In summary, we innovatively developed a regeneration process-matching scaffold with dynamic mechanical properties and spatial adaptability for collagen infiltration and remolding. The trajectory of PPDO, PGCL, and PGLA fibers was manipulated to optimize the dynamic

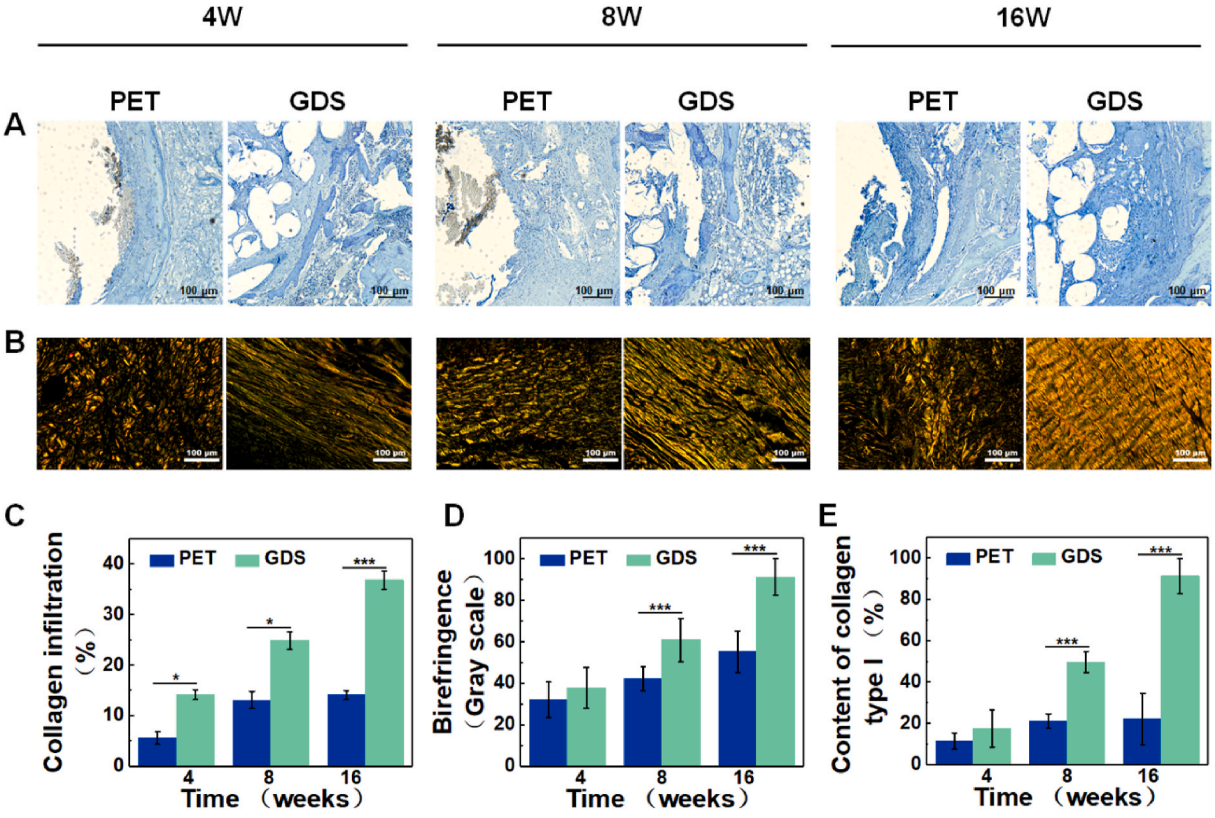


**Fig. 8.** Collagen regeneration evaluation. (A) Masson staining images, scale = 100 μm. (B) PSR staining images, scale = 100 μm. (C) Quantification of collagen infiltration. (D) The birefringence of collagen fibers. (E) Quantification of collagen type I.

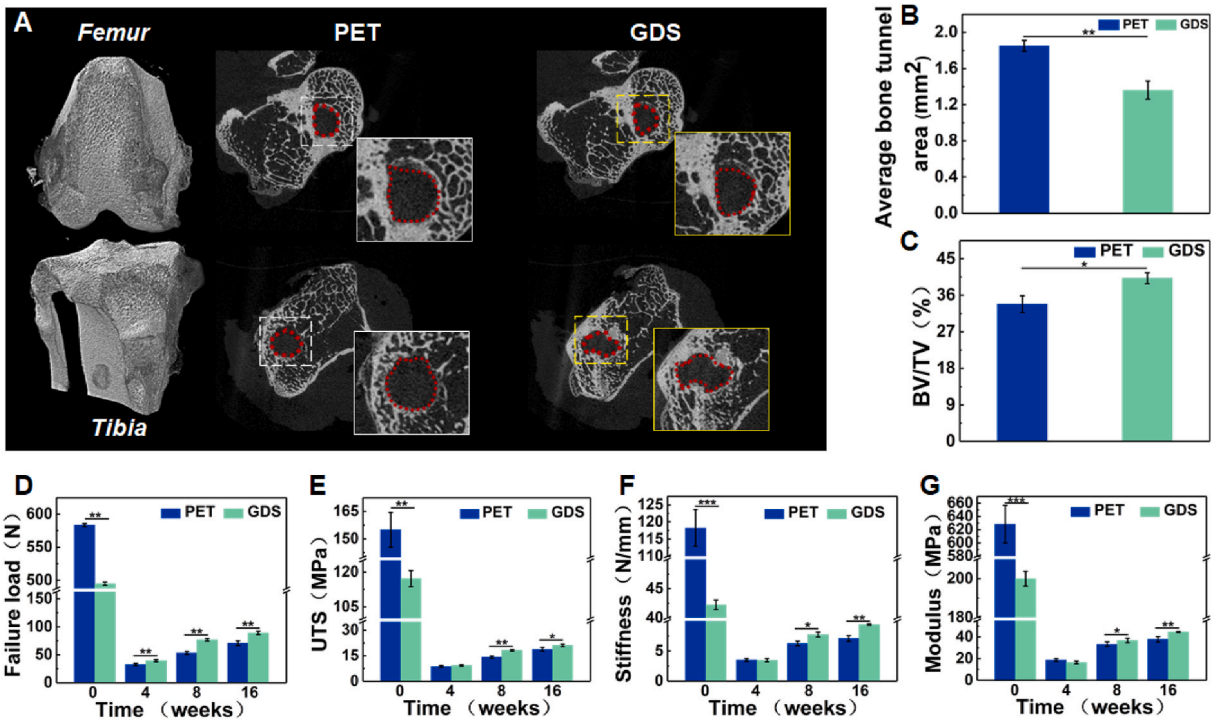


**Fig. 9.** (A) Micro-CT images of the cross-sections of the femoral and tibial bone tunnels in 16-week specimens, quantitative analysis of the (B) average bone tunnel area, and (C) BV/TV values. (D) Failure load, (E) UTS, (F) Stiffness, and (G) Modulus of the femur-graft-tibia complex after ACL reconstruction at 4, 8, and 16 weeks postoperatively in the PET and GDS scaffold.

mechanical properties and adaptive space. The GDS showed tri-phasic mechanical behavior and excellent strength. In this gradient degradation system, accompanied by the PGLA and PGCL degradation, the porosity of GDS gradually increased from day 6 until day 24. This was consistent with the cell proliferation and the matrix deposition phase during the healing process. *In vitro* data demonstrated that GDS exhibited great cytocompatibility and promoted the adhesion and proliferation for rTSPCs compared with the control scaffolds. *In vivo*, the histology staining revealed more collagen infiltration and better graft-to-bone integration in GDS, maintaining a failure load of 67.65% of the native ligament at 16 weeks. This regeneration process-matching scaffold could be a viable alternative to facilitate the reconstruction of ligaments and tendons. However, there is still much work to be done on biomaterials that can solve actual clinical problems. The mechanism of collagen infiltration mediated by internal space, the precise force value regulating collagen remodeling, the fine biomimetic structure (elongation at break, multi-scale structure from micro-scale to macro-scale), and the mechanical properties within 4 weeks should be considered in future research.

## Notes

The authors declare no competing financial interest.

## CRediT authorship contribution statement

**Xiaojing Xie:** Investigation, Methodology, Writing – original draft, Writing – review & editing. **Junjie Xu:** Methodology, Visualization. **Jing Lin:** Data curation, Investigation. **Jia Jiang:** Methodology. **Yunfan Huang:** Data curation. **Jun Lu:** Formal analysis. **Yuhao Kang:** Investigation. **Yage Hu:** Visualization. **Jiangyu Cai:** Visualization. **Fujun Wang:** Visualization. **Tonghe Zhu:** Supervision, Writing – review & editing, Funding acquisition. **Jinzhong Zhao:** Formal analysis, Funding acquisition. **Lu Wang:** Supervision, Funding acquisition, Validation.

## Declaration of competing interest

The authors declare that they have no known competing financial interests or personal relationships that could have appeared to influence the work reported in this paper.

## Acknowledgments

Xiaojing Xie and Junjie Xu contributed equally to this work. This work was supported by the National Key Research and Development Program of China (2018YFC1106200, 2018YFC1106201), the Fundamental Research Funds for the Central Universities (2232020G-01), and the 111 Project (BP0719035).

## Appendix A. Supplementary data

Supplementary data to this article can be found online at https://doi.org/10.1016/j.bioactmat.2021.11.001.

## References

[1] C.B. Frank, Ligament structure, physiology and function, J. Musculoskelet. Neuronal Interact. 4 (2) (2004) 199–201.
[2] S.L.Y. Woo, J.M. Hollis, D.J. Adams, R.M. Lyon, S. Takai, Tensile properties of the human femur-anterior cruciate ligament-tibia complex: the effects of specimen age and orientation, Am. J. Sports Med. 19 (3) (1991) 217–225.
[3] W. Amiel, D, C. Frank, F. Harwood, J. Fronek, Akeson, Tendons and ligaments: a morphological and biochemical comparison, J. Orthop. Res. 1 (3) (1983) 257–265.
[4] Y.J. No, M. Castilho, Y. Ramaswamy, H. Zreiqat, Role of biomaterials and controlled architecture on tendon/ligament repair and regeneration, Adv. Mater. 32 (18) (2020) 1904511.
[5] L. Chung, D.R. Maestas Jr., F. Housseau, J.H. Elisseeff, Key players in the immune response to biomaterial scaffolds for regenerative medicine, Adv. Drug Deliv. Rev. 114 (2017) 184–192.
[6] L.D. Huyer, S. Pascual-Gil, Y. Wang, S. Mandla, B. Yee, M. Radisic, Advanced strategies for modulation of the material-macrophage interface, Adv. Funct. Mater. 30 (44) (2020) 1909331.
[7] B.N. Brown, B.D. Ratner, S.B. Goodman, S. Amar, S.F. Badylak, Macrophage polarization: an opportunity for improved outcomes in and regenerative medicine, Biomaterials 33 (15) (2012) 3792–3802.

[8] N.L. Leong, F.A. Petrigliano, D.R. McAllister, Current tissue engineering strategies in anterior cruciate ligament reconstruction, J. Biomed. Mater. Res. 102 (5) (2014) 1614–1624.

[9] C. Frank, S.L.Y. Woo, D. Amiel, F. Harwood, M. Gomez, W. Akeson, Medial collateral ligament healing: a multidisciplinary assessment in rabbits, Am. J. Sports Med. 11 (6) (1983) 379–389.

[10] S.L.Y. Woo, M. Inoue, E. Mcgurk-Burleson, M.A. Gomez, Treatment of the medial collateral ligament injury: II: structure and function of canine knees in response to differing treatment regimens, Am. J. Sports Med. 15 (1) (1987) 22–29.

[11] D. Docheva, S.A. Müller, M. Majewski, C.H. Evans, Biologics for tendon repair, Adv. Drug Deliv. Rev. 84 (2015) 222–239.

[12] Z. Cai, Q. Saiding, L. Cheng, L. Zhang, Z. Wang, F. Wang, X. Chen, G. Chen, L. Deng, W. Cui, Capturing dynamic biological signals via bio-mimicking hydrogel for precise remodeling of soft tissue, Bioact. Mater. 6 (12) (2021) 4506–4516.

[13] J. Chen, J. Xu, A. Wang, M. Zheng, Scaffolds for tendon and ligament repair: review of the efficacy of commercial products, Expet Rev. Med. Dev. 6 (1) (2009) 61–73.

[14] M.F. Guidoin, Y. Marois, J. Bejui, N. Poddevin, M.W. King, R. Guidoin, Analysis of retrieved polymer fiber based replacements for the ACL, Biomaterials 21 (23) (2000) 2461–2474.

[15] H. Seitz, W. Pichl, V. Matzi, T. Nau, Biomechanical evaluation of augmented and nonaugmented primary repair of the anterior cruciate ligament: an in vivo animal study, Int. Orthop. 37 (11) (2013) 2305–2311.

[16] Z. Machotka, I. Scarborough, W. Duncan, S. Kumar, L. Perraton, Anterior cruciate ligament repair with LARS (ligament advanced reinforcement system): a systematic review, Sports Med. Arthrosc. Rehabil. Ther. Technol. 2 (1) (2010) 1–10.

[17] C.M. Glezos, A. Waller, H.E. Bourke, L.J. Salmon, L.A. Pinczewski, Disabling synovitis associated with LARS artificial ligament use in anterior cruciate ligament reconstruction a case report, Am. J. Sports Med. 40 (5) (2012) 1167–1171.

[18] H. Li, Z. Yao, J. Jiang, Y. Hua, J. Chen, Y. Li, K. Gao, S. Chen, Biologic failure of a ligament advanced reinforcement system artificial ligament in anterior cruciate ligament reconstruction: a report of serious knee synovitis, Arthrosc, J. Arthrosc. Relat. Surg. 28 (4) (2012) 583–586.

[19] Y. Li, X. Guo, S. Dong, T. Zhu, Y. Chen, S. Zhao, G. Xie, J. Jiang, H. He, C. Liu, A triple-coated ligament graft to facilitate ligament-bone healing by inhibiting fibrogenesis and promoting osteogenesis, Acta Biomater. 115 (2020) 160–175.

[20] L.M. Batty, C.J. Norsworthy, N.J. Lash, J. Wasiak, A.K. Richmond, J.A. Feller, Synthetic devices for reconstructive surgery of the cruciate ligaments: a systematic review, Arthrosc. J. Arthrosc. Relat. Surg. 31 (5) (2015) 957–968.

[21] V.I. Walters, A.L. Kwansa, J.W. Freeman, Design and analysis of braid-twist collagen scaffolds, Connect. Tissue Res. 53 (3) (2012) 255–266.

[22] A.B. Caruso, M.G. Dunn, Changes in mechanical properties and cellularity during long-term culture of collagen fiber ACL reconstruction scaffolds, J. Biomed. Mater. Res. 73 (4) (2005) 388–397.

[23] S. Cristino, F. Grassi, S. Toneguzzi, A. Piacentini, B. Grigolo, S. Santi, M. Riccio, E. Tognana, A. Facchini, G. Lisignoli, Analysis of mesenchymal stem dimensional HYAFF 11 (R)-based cells grown on a prototype ligament scaffold, J. Biomed. Mater. Res. 73 (3) (2005) 275–283.

[24] T. Masuko, N. Iwasaki, S. Yamane, T. Funakoshi, T. Majima, A. Minami, N. Ohsuga, T. Ohta, S.I. Nishimura, Chitosan-RGDSGGC conjugate as a scaffold material for musculoskeletal tissue engineering, Biomaterials 26 (26) (2005) 5339–5347.

[25] S. Yamane, N. Iwasaki, T. Majima, T. Funakoshi, T. Masuko, K. Harada, A. Minami, K. Monde, S. Nishimura, Feasibility of chitosan-based hyaluronic acid hybrid biomaterial for a novel scaffold in cartilage tissue engineering, Biomaterials 26 (6) (2005) 611–619.

[26] J.A. Cooper, H.H. Lu, F.K. Ko, J.W. Freeman, C.T. Laurencin, Fiber-based tissue-engineered scaffold for ligament replacement: design considerations and in vitro evaluation, Biomaterials 26 (13) (2005) 1523–1532.

[27] D.A. Brennan, A.A. Conte, G. Kanski, S. Turkula, X. Hu, M.T. Kleiner, V. Beachley, Mechanical considerations for electrospun nanofibers in tendon and ligament repair, Adv. Healthc. Mater. 7 (12) (2018) 1701277.

[28] A. Sensini, C. Gualandi, M.L. Focarete, J. Belcari, A. Zucchelli, L. Boyle, G.C. Reilly, A.P. Kao, G. Tozzi, L. Cristofolini, Multiscale hierarchical bioresorbable scaffolds for the regeneration of tendons and ligaments, Biofabrication 11 (3) (2019), 035026.

[29] A. Sensini, L. Cristofolini, Biofabrication of electrospun scaffolds for the regeneration of tendons and ligaments, Materials 11 (10) (2018) 1963.

[30] O.M. Bostman, H.K. Pihlajamaki, Adverse tissue reactions to bioabsorbable fixation devices, Clin. Orthop. Relat. Res. 371 (2000) 216–227.

[31] D.F.E. Ker, D. Wang, A.W. Behn, E.T.H. Wang, X. Zhang, B.Y. Zhou, Á.E. Mercado-Pagán, S. Kim, J. Kleimeyer, B. Gharaibeh, Functionally graded, bone-and tendon-like polyurethane for rotator cuff repair, Adv. Funct. Mater. 28 (20) (2018) 1707107.

[32] K. Chen, W. Zhang, T. La, P.A. Bastians, T. Guo, C. Cao, Microstructure investigation of plant architecture with X-ray microscopy, Plant Sci. 311 (2021) 110986.

[33] S. Elmarzougui, S. Ben Abdessalem, F. Sakli, Hysteresis measurement for characterising the dynamic fatigue of textile artificial ligaments, J. Text. Inst. 102 (2) (2011) 109–113.

[34] S. Turki, S. Marzougui, S. Ben Abdessalem, Impact of polyurethane yarns on the mechanical properties of braided artificial ligaments, J. Text. Inst. 106 (9) (2015) 912–918.

[35] S. Madhavarapu, R. Rao, S. Libring, E. Fleisher, Y. Yankannah, J.W. Freeman, Design and characterization of three-dimensional twist-braid scaffolds for anterior cruciate ligament regeneration, Technology 5 (2) (2017) 98–106.

[36] F.R. Noyes, J.L. DeLucas, P.J. Torvik, Biomechanics of anterior cruciate ligament failure: an analysis of strain rate sensitivity and mechanisms of failure in primates, J. Bone Jt. Surg. - Ser. A. 56 (2) (1974) 236–253.

[37] M. Ebrahimi, A. Mohammadi, A. Ristaniemi, L. Stenroth, R.K. Korhonen, The effect of different preconditioning protocols on repeatability of bovine ACL stress-relaxation response in tension, J. Mech. Behav. Biomed. Mater. 90 (2019) 493–501.

[38] M. Yamanaka, K. Yasuda, H. Tohyama, H. Nakano, T. Wada, The effect of cyclic displacement on the biomechanical characteristics of anterior cruciate ligament reconstructions, Am. J. Sports Med. 27 (6) (1999) 772–777.

[39] Y. Zhi, J. Jiang, P. Zhang, S. Chen, Silk enhances the ligamentization of the polyethylene terephthalate artificial ligament in a canine anterior cruciate ligament reconstruction model, Artif. Organs 43 (6) (2019) e94–e108.

[40] F. Yuan, W. Zhou, J. Cai, J. Zhao, X. Huangfu, F. Yin, Optimal graft length for anterior cruciate ligament reconstruction: a biomechanical study in beagles, Orthopedics 36 (5) (2013) e588–e592.

[41] F. Zhang, M.W. King, Biodegradable polymers as the pivotal player in the design of tissue engineering scaffolds, Adv. Healthc. Mater. 9 (13) (2020) 1901358.

[42] Y. Bi, D. Ehirchiou, T.M. Kilts, C.A. Inkson, M.C. Embree, W. Sonoyama, L. Li, A. I. Leet, B.M. Seo, L. Zhang, S. Shi, M.F. Young, Identification of tendon stem/progenitor cells and the role of the extracellular matrix in their niche, Nat. Med. 13 (10) (2007) 1219–1227.

[43] D. Nie, Y. Zhou, W. Wang, J. Zhang, J.H.-C. Wang, Mechanical overloading induced-activation of mtor signaling in tendon stem/progenitor cells contributes to tendinopathy development, Front. CELL Dev. Biol. 9 (2021) 687856.

[44] J. Cai, J. Xu, Y. Kang, Y. Li, L. Wang, X. Yan, J. Jiang, J. Zhao, Acceleration of ligamentization and osseointegration processes after anterior cruciate ligament reconstruction with autologous tissue-engineered polyethylene terephthalate graft, Ann. Transl. Med. 9 (9) (2021) 770.

[45] J. Cai, Q. Zhang, J. Chen, J. Jiang, X. Mo, C. He, J. Zhao, Electrodeposition of calcium phosphate onto polyethylene terephthalate artificial ligament enhances graft-bone integration after anterior cruciate ligament reconstruction, Bioact. Mater. 6 (3) (2021) 783–793.

[46] J. Jiang, F. Wan, J. Yang, W. Hao, Y. Wang, J. Yao, Z. Shao, P. Zhang, J. Chen, L. Zhou, S. Chen, Enhancement of osseointegration of polyethylene terephthalate artificial ligament by coating of silk fibroin and depositing of hydroxyapatite, Int. J. Nanomed. 9 (2014) 4569–4580.

[47] J. Cai, J. Wang, K. Ye, D. Li, C. Ai, D. Sheng, W. Jin, X. Liu, Y. Zhi, J. Jiang, J. Chen, X. Mo, S. Chen, Dual-layer aligned-random nanofibrous scaffolds for improving gradient microstructure of tendon-to-bone healing in a rabbit extra-articular model, Int. J. Nanomed. 13 (2018) 3481–3492.

[48] Y. Xu, S.W. Dong, Q. Zhou, X.M. Mo, L. Song, T.Y. Hou, J.L. Wu, S.T. Li, Y.D. Li, P. Li, Y.B. Gan, J.Z. Xu, The effect of mechanical stimulation on the maturation of TDSCs-poly(L-lactide-co-e-caprolactone)/collagen scaffold constructs for tendon tissue engineering, Biomaterials 35 (9) (2014) 2760–2772.

[49] D.B. Cohen, S. Kawamura, J.R. Ehteshami, S.A. Rodeo, Indomethacin and celecoxib impair rotator cuff tendon-to-bone healing, Am. J. Sports Med. 34 (3) (2006) 362–369.

[50] Q. Dong, J. Cai, H. Wang, S. Chen, Y. Liu, J. Yao, Z. Shao, X. Chen, Artificial ligament made from silk protein/Laponite hybrid fibers, Acta Biomater. 106 (2020) 102–113.

[51] L. Liu, Y. Zhang, C. Li, J. Cao, E. He, X. Wu, F. Wang, L. Wang, Facile preparation PCL/modified nano ZnO organic-inorganic composite and its application in antibacterial materials, J. Polym. Res. 27 (3) (2020) 78.

[52] C.G. McKenna, T.J. Vaughan, An experimental evaluation of the mechanics of bare and polymer-covered self-expanding wire braided stents, J. Mech. Behav. Biomed. Mater. 103 (2020) 103549.

[53] S. Marzougui, S. Ben Abdessalem, F. Sakli, Viscoelastic behavior of textile artificial, J. Appl. Sci. 9 (15) (2009) 2794–2800.

[54] B. Laycock, M. Nikolic, J.M. Colwell, E. Gauthier, P. Halley, S. Bottle, G. George, Lifetime prediction of biodegradable polymers, Prog. Polym. Sci. 71 (2017) 144–189.

[55] H.H. Lu, J.A. Cooper, S. Manuel, J.W. Freeman, M.A. Attawia, F.K. Ko, C. T. Laurencin, Anterior cruciate ligament regeneration using braided biodegradable scaffolds: in vitro optimization studies, Biomaterials 26 (23) (2005) 4805–4816.

[56] S. Shkarina, R. Shkarin, V. Weinhardt, E. Melnik, G. Vacun, P. Kluger, K. Loza, M. Epple, S.I. Ivlev, T. Baumbach, M.A. Surmeneva, R.A. Surmenev, 3D biodegradable scaffolds of polycaprolactone with silicate-containing hydroxyapatite microparticles for bone tissue engineering: high-resolution tomography and in vitro study, Sci. Rep. 8 (2018) 8907.

[57] Y. Fu, S. Liu, S.-J. Cui, X.-X. Kou, X.-D. Wang, X.-M. Liu, Y. Sun, G.-N. Wang, Y. Liu, Y.-H. Zhou, Surface chemistry of nanoscale mineralized collagen regulates periodontal ligament stem cell fate, ACS Appl. Mater. Interfaces 8 (25) (2016) 15958–15966.

[58] J. Zhang, B. Xie, Z. Xi, L. Zhao, L. Cen, Y. Yang, A comparable study of polyglycolic acid's degradation on macrophages' activation, Mater. Sci. Eng. C-Materials Biol. Appl. 109 (2020) 110574.

[59] L.S. Nair, C.T. Laurencin, Biodegradable polymers as biomaterials, Prog. Polym. Sci. 32 (8–9) (2007) 762–798.

[60] S. Farah, J.C. Doloff, P. Muller, A. Sadraei, H.J. Han, K. Olafson, K. Vyas, H.H. Tam, J. Hollister-Lock, P.S. Kowalski, M. Griffin, A. Meng, M. McAvoy, A.C. Graham, J. McGarrigle, J. Oberholzer, G.C. Weir, D.L. Greiner, R. Langer, D.G. Anderson, Long-term implant fibrosis prevention in rodents and non-human primates using crystallized drug formulations, Nat. Mater. 18 (8) (2019) 892–904.

[61] L. Gao, X. Liu, M. Xu, G. Sun, S. Xu, T. Zou, L. Wang, F. Wang, J. Da, Y. Wang, L. Wang, Biodegradable anti-biofilm fiber-membrane ureteral stent constructed

with a robust biomimetic superhydrophilic polycationic hydration surface exhibiting synergetic antibacterial and antiprotein properties, Small 17 (2021) 2006815.

[62] J. Cai, F. Wan, Q. Dong, J. Jiang, C. Ai, D. Sheng, W. Jin, X. Liu, Y. Zhi, S. Wang, Y. Sun, J. Chen, Z. Shao, S. Chen, Silk fibroin and hydroxyapatite segmented coating enhances graft ligamentization and osseointegration processes of the polyethylene terephthalate artificial ligament in vitro and in vivo, J. Mater. Chem. B. 6 (36) (2018) 5738–5749.

[63] H. Fan, H. Liu, E. Wong, S.L. Toh, J. Goh, In vivo study of anterior cruciate ligament regeneration using mesenchymal stem cells and silk scaffold, Biomaterials 29 (23) (2008) 3324–3337.